Field migration rates of tidal meanders recapitulate fluvial morphodynamics

Alvise Finotello[a], Stefano Lanzoni [b], Massimiliano Ghinassi[a], Marco Marani[b,c,d], Andrea Rinaldo[b,e,1], and Andrea D'Alpaos[a,1]

[a]Department of Geosciences, University of Padova, Padova, PD I-35131, Italy; [b]Department of Civil, Environmental, and Architectural Engineering, University of Padova, Padova, PD I-35131, Italy; [c]Nicholas School of the Environment, Duke University, Durham, NC 27708; [d]Department of Civil and Environmental Engineering, Duke University, Durham, NC 27708; and [e]Laboratory of Ecohydrology, École Polytechnique Fèdèrale Lausanne, CH-1015 Lausanne, Switzerland

The majority of tidal channels display marked meandering features. Despite their importance in oil-reservoir formation and tidal landscape morphology, questions remain on whether tidal-meander dynamics could be understood in terms of fluvial processes and theory. Key differences suggest otherwise, like the periodic reversal of landscape-forming tidal flows and the widely accepted empirical notion that tidal meanders are stable landscape features, in stark contrast with their migrating fluvial counterparts. On the contrary, here we show that, once properly normalized, observed migration rates of tidal and fluvial meanders are remarkably similar. Key to normalization is the role of tidal channel width that responds to the strong spatial gradients of landscape-forming flow rates and tidal prisms. We find that migration dynamics of tidal meanders agree with nonlinear theories for river meander evolution. Our results challenge the conventional view of tidal channels as stable landscape features and suggest that meandering tidal channels recapitulate many fluvial counterparts owing to large gradients of tidal prisms across meander wavelengths.

meander dynamics | sedimentary surfaces | tidal channels | remote sensing | tidal networks

Branching and meandering tidal channel networks are ubiquitous features of tidal landscapes that control water, sediment, and nutrient fluxes therein (1–3) (Fig. 1*A*). Particularly, meandering exerts a prominent influence on both the dynamics of tidal channels and the stratigraphy of the platforms they cut through, thus possibly leading to sedimentary patterns with complex stratal architectures (2, 4). Despite their extensive presence and importance in landscape evolution, tidal meanders have received comparably less attention than their fluvial counterparts (5–9). The large amount of studies on fluvial meanders (10–12) is, in fact, counterbalanced by relatively few papers which analyze the geometrical properties of tidal meanders, as well as their dynamic evolution, documented in terms of field observations, numerical modeling, and laboratory experiments (13–16). Moreover, although tidal meanders are uniquely characterized by periodically reversing flows, their planform dynamics (17, 18) and related sedimentary deposits (2, 19, 20) have typically been approached using theories assuming a basic similarity with fluvial meanders (14, 18). The reliability of this assumption might, however, be challenged by the slow planform dynamics exhibited by tidal meanders, whose migration rates in the order of centimeters per year (17, 21) appear to be at odds with the generally high mobility characterizing their fluvial counterparts, the latter migrating meters or even up to tens of meters per year (22, 23). The stability of tidal meanders has been traditionally justified by invoking the bank-stabilizing role played by cohesive sediments (15), dense halophytic-vegetation roots (21), and persisting slump blocks along channel flanks (17, 18), as well as by speculation that migration might be hindered by the mutually balanced effect of opposite bidirectional flows (14). Therefore,

despite the remarkable differences in the physical processes they are shaped by, tidal meanders are generally seen as the slowly migrating version of fluvial meanders. This hypothesis seems to be further supported by the presence, in the tidal framework, of fluvial-like migration features such as meander cutoffs (20) (Fig. 1), which might, however, be diagnostic of strongly migrating meanders as well. Similarly, if on the one hand the presence of slump blocks is thought to protect banks from further erosion (17, 24, 25), on the other hand it undeniably represents a proxy of actively migrating channels. Despite clear signs of active migration (Fig. 1*B*), the general consensus is that tidal meanders are relatively stable landscape features, and it is therefore essential that this paradox be clarified to improve our understanding of tidal depositional environments.

Here, we investigate migration rates and dynamics of tidal meanders by means of field observations and modeling interpretation of saltmarshes at San Felice, within the Lagoon of Venice, Italy (Fig. 1*A* and *SI Appendix, Study Area*). To assess tidal-meander dynamics, their migration rates are first estimated, for a limited number of ground-truthing pilot meanders, from the stratigraphic record (Fig. 1*C* and *Materials and Methods*). To obtain statistically significant data, migration rates are then accurately calculated by analyzing a sequence of high-resolution orthophotos of the study area over a significant time frame. Two methods are applied to determine meander migration rates (*Materials and Methods*): the best-fitting circle (BFC) (23) and

Significance

Meandering tidal channel networks play a central role in the ecomorphodynamic evolution of the landscapes they cut through. Despite their ubiquitous presence and relevance to sedimentary and landscape features, few observations of tidal-meander evolution exist, and we lack a full understanding of the governing processes. Field analyses show that tidal meanders, traditionally viewed as stable landscape features, display modes of migration and migration rates per unit width quite similar to those characterizing their fluvial counterparts, with important implications for the characterization of the related sedimentary products. The results presented here contribute to our understanding of the morphological evolution of tidal landscapes.

EARTH, ATMOSPHERIC, AND PLANETARY SCIENCES

Fig. 1. Overview of the study area and example of tidal-meander migration and dynamics. (*A*) The San Felice saltmarsh area, in the Northern Venice Lagoon, Italy. Study case bends are highlighted in green. (*B*) Example of the evolution that tidal channels in the study area have undergone over the last 50 y. Black dots indicate the location of the sedimentary cores used to determine the migration rates from sedimentological analyses. (*C*) Example of main sedimentary surfaces identified from sedimentological analyses carried out over the abandoned meander loop highlighted in *B*. (*D*) Detailed sedimentological core data of *C*.

the homologous points (HP) methods. While the former represents a method widely used in the literature of riverine meanders (23, 26), the latter is a unique procedure to objectively characterize meander migration and planform features. Results are compared with the theory of fluvial meanders (6, 7, 10, 11, 27) by analyzing spectral properties of empirical tidal-channel curvature.

Results and Discussion

Sedimentological analyses carried out on several tidal-meander bends in the study area (Fig. 1*B*) provide migration rates of the order of $\zeta = 0.08–0.20$ m/y, which are consistent with the values obtained from both the BFC method ($\zeta = 0.16 \pm 0.19$ m/y) and the HP method ($\zeta = 0.20 \pm 0.22$ m/y), as well as with those obtained for the New Jersey wetlands (21) ($\zeta = 0.21 \pm 0.11$ m/y), although the latter refer to the migration of whole tidal channels rather than to single meanders. A poor correlation is observed between migration rates and channel-width variations (*SI Appendix, Meander Migration*), thus excluding the hypothesis that the observed migration rates are simply due to channel broadening, driven by increased tidal prism (28), rather than to real meander dynamics. On the one hand, our results seem to confirm the relative planform stability of tidal meanders compared with migration rates, typical of alluvial rivers, ranging from a few to tens of meters per year (23, 29, 30). On the other hand, a convenient scaling should be applied to avoid misleading comparisons. Therefore, using a classic standard for fluvial realms (12, 22, 29, 31–33), we have normalized migration rates by channel width ($\zeta^* = \zeta/B$ [y^{-1}]) and plotted them vs. the dimensionless ratio between radius of curvature and width ($R^* = R/B$). According to the BFC method (Fig. 2*A*), the distribution of meander migration rates (ζ^*) in the $\{R^*; \zeta^*\}$ plane is enveloped by a bell-shaped curve, which can be interpreted as the maximum potential migration rate (12) as a function of bend curvature. Starting from low values of R^*, the potential migration rate grows rapidly, reaching a maximum at $2 < R^* < 3$, followed by a gentle decrease for values of $R^* > 3$. The presence of a potential-migration peak at $2 < R^* < 4$ is a common feature of meandering rivers (22, 23, 30, 31, 34, 35), and its occurrence is likely dic-

tated by two competing processes that reduce (enhance) ζ^* for small (large) values of R^* and vice versa. Strong channel curvature enhances both the secondary flow and the phase lag between near-bank velocity and the curvature itself (35–38), thus resulting in more pronounced outer-bank erosion and migration. Nevertheless, in sharply curved bends ($R^* < 2$), whose lengths are typically short since high curvatures are unlikely to be sustained over long distances (32), the near-bank velocity maximum tends to occur at the downstream end of the bend (35), thus preventing bends from growing further. Moreover, in very sharp bends the increase in curvature-induced secondary flow is limited by the growth of hydrodynamic nonlinearities, such as secondary-flow saturation and amplification of the outer-bank cell rotating in the opposite direction to the main secondary cell (33), that cause energy losses and reduce erosion rates. The migration rates per unit width (ζ^*) of tidal meanders presented here display magnitudes of maximum, median, and 90th percentile values comparable to those that Lagasse et al. (23) observed from a total of 89 rivers by applying the same methodology (Fig. 2 *B* and *C*). Indeed, we performed a two-sided Kolmogorov–Smirnov (KS) test to verify the null hypothesis that the observed tidal and fluvial ζ^* come from the same distribution at a significance level $\alpha = 0.05$ (P value = 0.23). Our results therefore suggest that, when scaled by channel width, tidal and fluvial meanders exhibit quite similar migration rates, thus challenging the notion that tidal channels are slowly evolving landscape features (17). In addition, the bivariate KDEs of ζ^* and R^* display quite similar patterns (Fig. 2 *A* and *B*, *Insets* and *SI Appendix*, Fig. S10). Indeed, although bends with $2 < R^* < 3$ are suggested to migrate at high rates (12, 22, 29), displaying the highest potential for migration, data are generally clustered around relatively low values of both ζ^* and R^*, the highest kernel density values being centered at $R^* = 1$ and $\zeta^* = 0.01$ y^{-1}. The wide scatter displayed by migration rates for a given range of R^* can be interpreted as the manifestation of the presence of a whole family of curves (31) characterized by different hydrodynamics and other local parameters, such as sediment grain size (31), bank erodibility (33), and floodplain heterogeneity (39), as well as abundance and type of
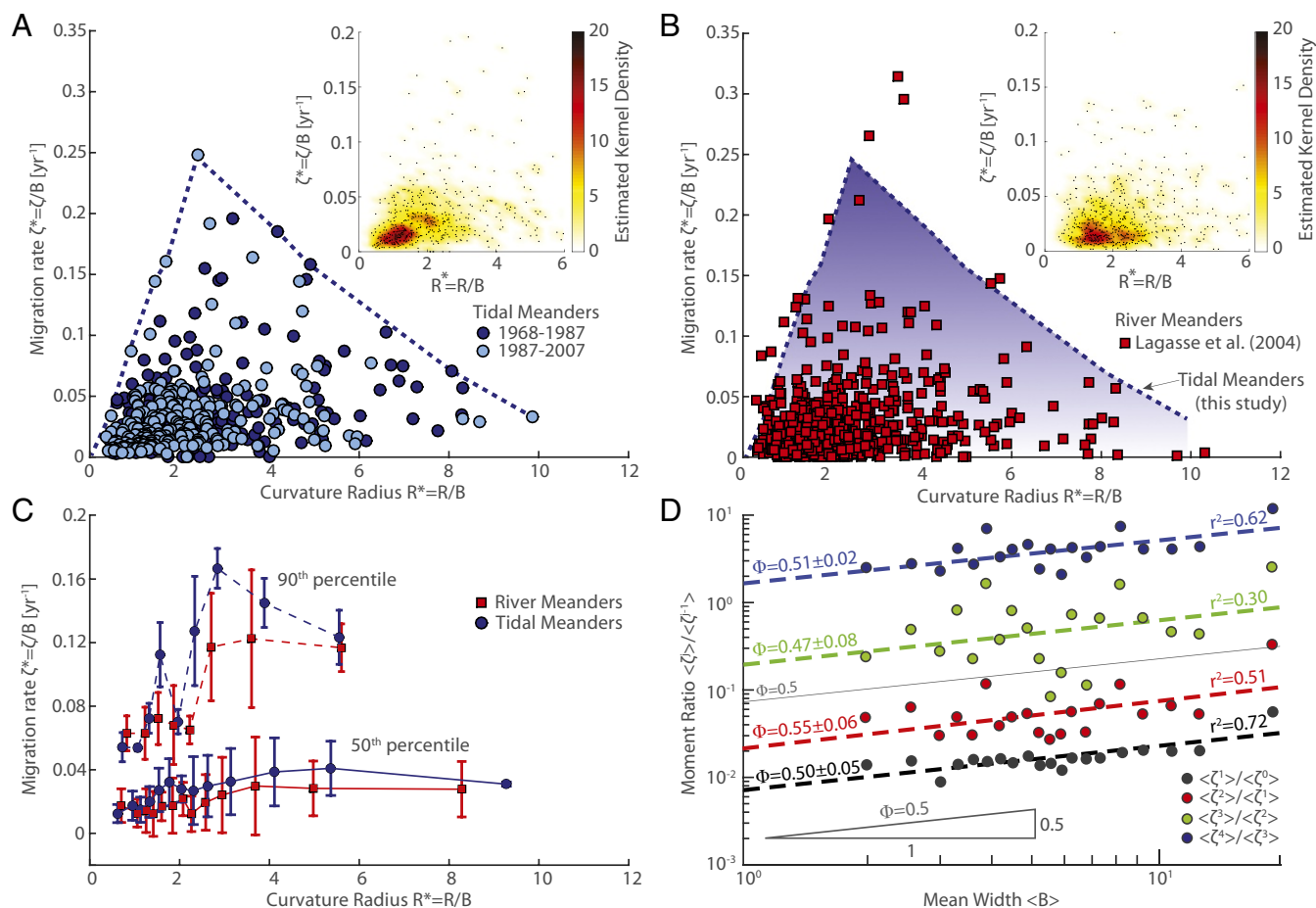
Fig. 2. Migration rates as a function of bend curvature characterized through the BFC method. (*A*) Migration rates per unit width (ζ^*) are plotted vs. the dimensionless radius of curvature (R^*) of tidal meanders for the two considered periods (1968–1987 and 1987–2007). (*B*) ζ^* vs. R^* data, for fluvial settings derived from Lagasse et al. (23), are plotted together with the envelope curve calculated for tidal meanders. *Insets* in *A* and *B* contain the 2D kernel density estimates (KDEs) of the data (obtained by considering a Gaussian kernel and bandwidths equal to 0.25 R^* and 0.01 ζ^*). (*C*) Comparison between the 50th and 90th percentiles of migration rates per unit width of tidal and fluvial meanders. Binned averaged values are obtained by averaging sets of 50 and 80 data for the 50th and 90th percentiles, respectively. Bar lengths represent 1 SD. (*D*) Ratios of successive moments of ζ distribution are plotted against the mean width $\langle B \rangle$ for each of the $k = 20$ width classes calculated from our dataset; dashed lines represent linear regressions on log-transformed data. Slopes (Φ) and correlation coefficients (r^2) of the linear regression lines are also reported, together with Φ-error range calculated by a standard bootstrap resampling method. Vertical offset is arbitrary.

vegetation (21), which are crucial in determining actual migration rates. Moreover, it has been illustrated (32) that local migration rates, ζ^*, are not simply related to the local bend curvature, being ζ^* dependent also on the curvature convolution upstream and downstream of the considered bend (i.e., on the position of a bend within a meander train) (9, 32, 38, 40, 41), as well as on bend length, which must be sufficiently large to allow secondary flows to fully develop. Nonetheless, local migration rates are intrinsically a random variable. Finite-size scaling analysis allows one to identify the functional dependence on the physical quantity that limits the upper values, regardless of the fluctuations due to local heterogeneity (42). We have binned observed tidal meanders into 20 classes according to sample size, labeling each bin with the average width $\langle B \rangle$ to sort out broad features of the probability distribution $p(\zeta|B)$ (*Material and Methods*). It can be shown (42) that if the ratio of the moments of different order, i.e., $\langle \zeta^n \rangle / \langle \zeta^{n-1} \rangle$, scales with $\langle B \rangle$ for every n, then the distribution is of the type $p(\zeta|B) = \zeta^{-\phi} \cdot \mathbf{F}(\zeta/\langle B \rangle^{\Phi})$, where $\mathbf{F}$ is a function that does not need to be specified (*Materials and Methods*). Fig. 2*D* emphasizes that the scaling of the moments is remarkably consistent with the above form. A proper check shows that $\Phi = 0.5 \pm 0.04$ (*Materials and Methods*). We thus conclude that

the maximum local migration rates are proportional to $B^{0.5}$ (having assumed as the actual value of B the midpoint of the binning class of the field values). Thus, the logical sequence for the interpretation of tidal-meander geomorphology is as follows: The local cross-sectional area, Ω, of the tidal channel is determined by landscape-forming discharges Q, which in turn are determined by the tidal prism P via the O'Brien–Jarrett–Marchi law (28) [$\Omega \propto P^\alpha \propto Q^\gamma$, where α, γ are well-studied empirical coefficients (28, 43)] (*SI Appendix, On the Tidal Prism–Channel Width Relationship*).

Given earlier findings on the width-to-depth ratio in tidal channels of various sizes (13, 44), our results firmly establish that meander migration rates are limited by the local tidal prism via a fluvial-like landscape-forming discharge proportional to $B^{0.5}$. The ever-increasing, along-channel spatial changes in the tidal prism across meander wavelengths (*SI Appendix*, Fig. S9) thus suggest that tidal meanders recapitulate fluvial meanders by essentially replicating the same physical mechanism in a rapidly accelerated spatial sequence. Although the BFC method is an effective tool for characterizing meandering channel migration, it suffers from both the subjectivity in the choice of points defining a whole meander and the possibility of representing only

the overall behavior of a bend. To objectively identify individual meander bends and provide a spatially continuous characterization of local migration rates, we developed a unique methodology, named the HP method (*Materials and Methods*). The maximum migration rates per unit width, ζ^*, computed through the HP method and plotted as a function of the dimensionless radius, R^*, display a pattern similar to that obtained through the BFC method, with a peak in the potential migration rate for $2 < R^* < 3$ that is mainly determined by the migration rates of meander apical points (Fig. 3*A*). The local migration rates estimated through the HP method can be up to two times larger than the meander-averaged migration rates obtained with the BFC method (in particular, bend apex points exhibit maximum and mean migration rates equal to $\zeta^*_{A_{MAX}} = 0.62$ y^{-1} and $\langle \zeta^*_A \rangle = 0.35$ y^{-1}, respectively). On the other hand, points other than the bend apexes exhibit a distribution of migration rates characterized by a relatively smoother peak in the range $5 < R^* < 6$ and a heavier right tail (Fig. 3*B*). Although tidal meanders are shaped by bidirectional flows (2), potentially leading to planform features distinct from those of terrestrial rivers, no substantial differences between tidal and fluvial meander migration rates emerge from our results. A possible explanation lies in the fact that in tidal landscapes either flood or, more commonly, ebb flows dominate the landscape formation processes (45, 46), thus preferentially shaping meanders and their planforms in a way analogous to that of their fluvial counterparts. The violin plot of the binned migration rates (Fig. 3*C*) provides information on the probability distribution of ζ^* for given intervals of bend-curvature values. Two peaks are observed for R^* in the ranges $2 < R^* < 3$ and $5 < R^* < 6$, representing the set of data relative to the apex points and all of the other points, respectively. Both the mean and the median of the distributions slightly increase for values of R^* up to 4 and then attain an almost constant value around 0.05 y^{-1} and 0.04 y^{-1}, respectively. In agreement with the limited existing literature (17), a value of $\langle \zeta^* \rangle = 0.45\%$ y^{-1} is found. Further comparisons between fluvial and tidal meandering pattern dynamics have been carried out by analyzing the spectral properties of the observed channel patterns. A well-established framework developed in the fluvial setting expresses meander curvature in terms of a sine-generated curve (5, 6, 47). By Fourier transforming the curvature signal (13), the relationships between the various harmonics of the curvature spectrum, meander migration, and sinuosity can be evaluated. The majority of spectral power density is generally contained along the first harmonic, although in some cases higher-order harmonics prevail (*SI Appendix*, Fig. S8). While the first-order harmonic results in simple, sine-generated curves, its interactions with higher-

order harmonics cause a progressive fattening and skewing of the meander shape, increasing its planform sinuosity (37, 47). High-order harmonics are, in turn, known to develop during meander evolution, their presence indicating a mature, highly sinuous meander.

However, for no specific meander bend was such an evolutionary pathway completely observable from our dataset, given the relative limitedness of the considered time span. We have therefore inferred the development stage of every individual meander by considering its dominant harmonic (K), that is, the harmonic containing the largest fraction of total power density. This provides us a meaningful, first approximation of meander maturity. Our analysis indicates (Fig. 4*A*) that when the first harmonic is dominant, the mean meander-averaged migration rate is about 0.13 m/y. This value increases to a maximum close to 0.20 m/y when the second harmonic becomes dominant, and it subsequently decreases for dominant harmonics of higher order. A similar pattern is also observed when analyzing meander sinuosity (σ) as a function of the dominant harmonic: In this case, σ reaches its maximum when the third harmonic dominates (Fig. 4*A*; see *SI Appendix, Curvature Spectra* for further details). These observations agree with those for nonlinear, river-meander models (10, 24, 37, 48), showing that (*i*) bend growth rate increases to a peak and then slowly decays as a meander progressively evolves, producing higher-order harmonics; (*ii*) the formation of the third harmonic in a curvature spectrum is related to a sharp increase in meander sinuosity; and (*iii*) the growth in meander sinuosity is eventually interrupted as the meander cuts off or stabilizes. Note that the tidal meander-averaged migration rate per unit width decreases for increasing meander sinuosity (Fig. 4*B*), suggesting that well-developed, sinuous tidal meanders are typically more stable, a behavior that also characterizes their fluvial counterparts (Fig. 4*B*, *Inset*). Our results suggest that, although key differences between fluvial and tidal meanders can be identified, particularly on the occurrence of bidirectional flows shaping the latter, tidal meanders display migration rates per unit width of the same magnitude as those of their fluvial counterparts. Moreover, the migration dynamics of tidal channels can be at least qualitatively described by the theoretical relationship between migration rates and curvature-spectrum harmonics developed for fluvial settings. Nonetheless, the process of meander migration in fluvial environments might lead to the development of different planform morphologies relative to the tidal case. In tidal landscapes, in fact, network drainage density is typically higher than in fluvial ones (49, 50) and channel confluences are more frequent, thus preventing in many cases migrating meanders from fully developing into a cutoff without connecting
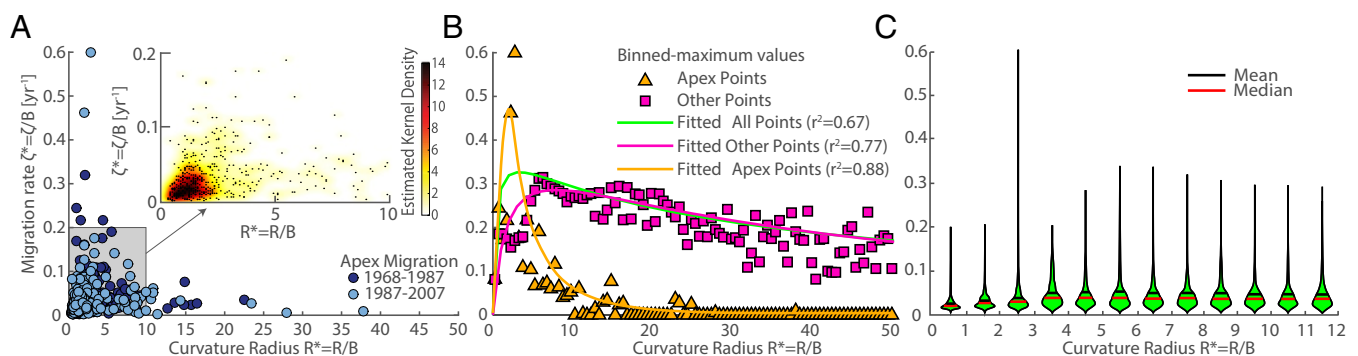
Fig. 3. Continuous characterization of meander migration rates on the basis of the HP method. (*A*) Migration rates per unit channel width (ζ^*) are plotted vs. the dimensionless radius of curvature (R^*). *A, Inset* contains a 2D KDE of the displayed data (Gaussian kernel, bandwidths 0.25 R^* and 0.01 ζ^*). For the sake of clarity, only results for apex points are entirely represented. (*B*) Maximum binned migration rates observed for both apexes and points other than the apexes. A lognormal function yields the best fit to these binned values of the migration rates. Correlation coefficients (r^2) are also reported. (*C*) Violin plots of ζ^*-binned values. The mean (black lines) and the median (red lines) of the distributions are also shown.
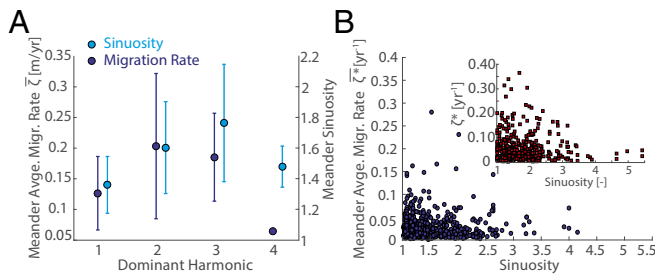
Fig. 4. Relationship between tidal-meander migration rates and curvature-spectrum harmonics. (*A*) Meander-averaged migration rates vs. meander dominant harmonics and meander sinuosity vs. meander dominant harmonics. Dots represent the mean migration rate and the mean meander sinuosity for each harmonic. Bar length corresponds to 1 SD. (*B*) Meander-averaged migration rates per unit width vs. meander sinuosity for tidal meanders. (*B*, *Inset*) Meander migration rates per unit width vs. meander sinuosity for the 20 rivers with highest reach sinuosity described in Lagasse et al.'s (23) database.

to other adjoining active channels. On the contrary, rivers can freely wander through alluvial valleys, promoting the formation of cutoffs strewn across the landscape. Signatures of meander cutoffs are also less frequently detected, possibly due to the smaller size of tidal channels, the dense vegetation through which they evolve, and the high rates of mud accumulation typical of saltmarsh platforms (51) that might hide the scars of cutoffs. We also show that tidal-meander migration is controlled by local channel width, a proxy for the landscape-forming prism whose large spatial gradients are a defining feature of tidal landscapes. These results bear important consequences for the understanding of estuarine landscape evolution, with implications of interest to scientists across the geosciences, due to the critical role exerted by branching and meandering channels on geomorphic, ecological, and sedimentary patterns.

Materials and Methods

Migration from the Stratigraphic Record. Using an Ejikelkamp hand auger with an extendable handle, through a gouge sampler with a length of 1 m and a diameter of 30 mm, sediment cores were collected along the axis of different point-bar deposits in the study-site area (Fig. 1*B*), with core depths ranging from 1 m to 3 m to include the whole thickness of point-bar deposits (20, 52, 53). The topography of this area and the location of the stratigraphic cores were surveyed through a differential GPS (Leica CS15) in RTK modality, with a vertical precision of ± 0.02 m. Core logging, carried out following the basic principles of facies analyses, allowed for reconstructing the key sedimentary surfaces (20, 52, 53) (Fig. 1*C*). The time span over which the considered point bar has evolved can be determined as $t_e = s_t/s_a$, where s_t is the thickness of saltmarsh deposits accumulated during bar migration and $s_a = 2.5$ mm/y is the local saltmarsh accretion rate in equilibrium with the rate of sea-level rise (54). The migration rate of the considered bend can be determined as $\zeta = d/t_e$, where d is the distance covered by the channel thalweg during point-bar migration. In the study case illustrated in Fig. 1*C* (main sedimentary surfaces) and Fig. 1*D* (detailed core logs), s_t and d are equal to 0.45 m and 14.0 m, respectively, corresponding to $t_e = 180$ y, finally resulting in a migration rate of $\zeta = 0.08$ m/y. Migration rates computed for the other ground-truthing pilot meanders are in the range 0.08–0.20 m/y.

Migration Rates from Aerial Photos. We used three sets of aerial photographs (*SI Appendix*, Fig. S1) acquired in 1968, 1987, and 2007 of tidal channels dissecting the San Felice saltmarsh, in the Venice Lagoon. All images were georeferenced to an accuracy of ± 0.1 m (with an estimated error in the migration rates of about 5% over a 20-y period), and the pairs of images (1968–1987 and 1987–2007) were superimposed to obtain a map of changes in the position of channel banks. We selected only bends which were included and clearly detectable in all of the photos, to prevent misleading results due to the incorrect identification of channel banks. Banks of chosen meanders were first digitized in a geographic information system environment: Where a bifurcation of the network occurred, digitalization was continued only for the major reach, whereas a new digitalization was

started for minor lateral tributaries. Two methods were used to compute migration rates from the aerial photos: the BFC method and the HP method described in the following text.

BFC method. Every meander bend is described by a series of delineation points, and the center coordinates $\{x_{c_B}; y_{c_B}\}$ and radius R_B of the best-fitting circle are computed by solving a linear system (23). The comparison of two different planar configurations at times t and $t + \Delta t$ allows us to calculate both bend translation and expansion. The latter corresponds to the variation of bend radius $\Delta R = R_B(t + \Delta t) - R_B(t)$, whereas the former is calculated as $\Delta S = \sqrt{(\Delta x_c)^2 + (\Delta y_c)^2}$, where $\Delta x_c = x_{c_B}(t + \Delta t) - x_{c_B}(t)$ and $\Delta y_c = y_{c_B}(t + \Delta t) - y_{c_B}(t)$. The rate of migration is finally computed as $\zeta_B = \sqrt{\Delta S^2 + \Delta R^2}/(\Delta t)$. Meander Cartesian wavelength (L_{xy}) and amplitude (A) are also measured, as well as meander width (B) in correspondence to both the inflexion and apex points, with the latter used to normalize migration rates to carry out a direct comparison with fluvial data (23) (see *SI Appendix, Meander Migration* for further details).

HP method. We apply a well-developed technique (13) to objectively identify and continuously characterize tidal-meander geometry, which is based on a mathematical definition of the curve $\Gamma(s) = \{x(s); y(s)\}$, where x and y are the Cartesian coordinates of the arbitrary point of the channel axis and s is its intrinsic coordinate, assumed to be positive if directed landward. The curvature $C(s)$ [L^{-1}] is therefore calculated as (13)

$$C = -\frac{d\theta}{ds} = \left[\frac{dx}{ds}\frac{d^2y}{ds^2} - \frac{dy}{ds}\frac{d^2x}{ds^2}\right] \cdot \left[\left(\frac{dx}{ds}\right)^2 + \left(\frac{dy}{ds}\right)^2\right]^{-3/2}, \qquad [1]$$

where θ is the angle between the tangent to the channel axis and an arbitrarily selected reference direction. A Savitzky–Golay low-pass filter is applied to smooth noises in the curvature signal (18). Locations of both inflexion (s_i) and apex (s_a) points are identified as null curvature points ($C(s_i) = 0$) and local curvature maxima ($C(s_a) = C_{MAX}$), respectively, thus allowing one to identify individual meander bends. Geometrical features, such as channel width ($B(s)$) and meander intrinsic wavelength (L_s), are computed along the intrinsic coordinate s, while the Cartesian wavelength (L_{xy}) is defined by the distance between the initial and the final section of the meander in the $\{x; y\}$ plane. Meander sinuosity is defined as $\sigma = L_s/L_{xy}$. To compute migration rates, every meander bend is first divided into a series of $N = 100$ equally spaced points, including the apex point. The meander reach included between the apex and the most landward (seaward) inflexion point is therefore divided into $(N/2) - 1$ branches. The displacement of the nth point (δ_n) is calculated as the homologous point distance between the initial (at time t) and the final (at time $t + \Delta t$) channel planform configuration:

$$\delta_n = \sqrt{[x_n(t + \Delta t) - x_n(t)]^2 + [y_n(t + \Delta t) - y_n(t)]^2}. \qquad [2]$$

The migration rate ζ_n of the nth point is finally determined as the $\zeta_n = \delta_n/\Delta t$.

On the Scaling of Tidal Meander Migration Rates. According to the apex width of every individual meander, we have binned our study-case bends into $k = 20$ classes, each of them containing 24 individual bends. Provided that $p_k(\zeta)$ represents the probability distribution of migration rates for a given class k with migration rates belonging to $[\zeta, \zeta + d\zeta)$ (55), we tested whether $p_k(\zeta)$ exhibits a finite-size scaling in the form $p(\zeta|B) = \zeta^{-\phi} \cdot F(\zeta/\langle B\rangle^\Phi)$, where $\langle B\rangle$ is the average width of a given k class, and F is a suitable scaling function, common to all of the k classes, whose specification is not necessary for our purposes (55). A test for the validity of the assumption that $p(\zeta|B) = \zeta^{-\phi} \cdot F(\zeta/\langle B\rangle^\Phi)$ is represented by the proportionality of successive moments of ζ ($\langle\zeta^n\rangle/\langle\zeta^{n-1}\rangle$, $n > 1$) to $\langle B\rangle$ [for further details see Giometto et al. (55)]. Fig. 2*D* indeed shows successive moment ratios calculated from our data and the corresponding linear regression lines of log-transformed data. The slopes of these lines consistently exhibit a value of $\Phi = 0.5 \pm 0.04$.

1. Coco G, Zhou Z, van Maanen B, Olabarrieta M, Tinoco R (2013) Morphodynamics of tidal networks: Advances and challenges. *Mar Geol* 346:1–16.
2. Hughes ZJ (2012) Tidal channels on tidal flats and marshes. *Principles of Tidal Sedimentology*, eds Davis RA, Dalrymple RW (Springer, New York), pp 269–300.
3. D'Alpaos A, Lanzoni S, Marani M, Fagherazzi S, Rinaldo A (2005) Tidal network ontogeny: Channel initiation and early development. *J Geophys Res* 110:1–14.
4. Barwis JH (1978) Sedimentology of some South Carolina tidal-creek point bars, and a comparison with their fluvial counterpart. *Fluvial Sedimentology*, ed Miall AD (Canadian Society of Petroleum Geologists, Calgary, AB, Canada), pp 129–160.
5. Leopold LB, Langbein W (1966) River meanders. *Sci Am* 71:60–70.
6. Ikeda S, Parker G, Sawai K (1981) Bend theory of river meanders. Part 1. Linear development. *J Fluid Mech* 112:363–377.
7. Parker G, Sawai K, Ikeda S (1982) Bend theory of river meanders. Part 2. Nonlinear deformation of finite-amplitude bends. *J Fluid Mech* 115:303–314.
8. Dietrich WE, Smith JD (1984) Bed load transport in a river bend. *Water Resour Res* 20:1355–1380.
9. Howard AD, Knutson TR (1984) Sufficient conditions for river meandering: A simulation approach. *Water Resour Res* 20:1659–1667.
10. Zolezzi G, Luchi R, Tubino M (2012) Modeling morphodynamic processes in meandering rivers with spatial width variations. *Rev Geophys* 50:1–24.
11. Seminara G (2006) Meanders. *J Fluid Mech* 554:271–297.
12. Hooke JM (2013) River meandering. *Treatise on Geomorphology*, ed Wohl E (Academic, San Diego), Vol 9, pp 260–288.
13. Marani M, Lanzoni S, Zandolin D, Seminara G, Rinaldo A (2002) Tidal meanders. *Water Resour Res* 38:7-1–7-14.
14. Solari L, Seminara G, Lanzoni S, Marani M, Rinaldo A (2002) Sand bars in tidal channels. Part 2. Tidal meanders. *J Fluid Mech* 451:203–238.
15. Kleinhans M, Schuurman F, Wiecher B, Markies H (2009) Meandering channel dynamics in highly cohesive sediment on an intertidal mud flat in the Westerschelde estuary, The Netherlands. *Geomorphology* 105:261–276.
16. Tambroni N, Luchi R, Seminara G (2017) Can tide dominance be inferred from the point bar pattern of tidal meandering channels? *J Geophys Res* 122:492–512.
17. Gabet EJ (1998) Lateral migration and bank erosion in a saltmarsh tidal channel in San Francisco Bay, California. *Estuaries* 21:745–753.
18. Fagherazzi S, Gabet EJ, Furbish DJ (2004) The effect of bidirectional flow on tidal channel planforms. *Earth Surf Process Landforms* 29:295–309.
19. Choi K, Jo JH (2015) Morphodynamics of tidal channels in the open coast macrotidal flat, Southern Ganghwa Island in Gyeonggi Bay, West Coast of Korea. *J Sedim Res* 85:582–595.
20. Brivio L, et al. (2016) Aggradation and lateral migration shaping geometry of a tidal point bar: An example from salt marshes of the Northern Venice Lagoon. *Sedim Geol* 143:141–155.
21. Garofalo D (1980) The influence of wetland vegetation on tidal stream channel migration and morphology. *Estuaries* 3:258–270.
22. Hudson PF, Kessel RH (2000) Channel migration and meander-bend curvature in the lower Mississippi River prior to major human modification. *Geology* 28:531–534.
23. Lagasse PF, Zevenbergen L, Spitz W, Thorne C (2004) *A Methodology for Predicting Channel Migration: NCHRP Project No. 24-16* (Ayres Associates, Fort Collins, CO), Vol 67.
24. Parker G, et al. (2011) A new framework for modeling the migration of meandering rivers. *Earth Surf Process Landforms* 36:70–86.
25. Eke EC, Parker G, Shimizu Y (2014) Numerical modeling of erosional and depositional bank processes in migrating river bends with self-formed width: Morphodynamics of bar push and bank pull. *J Geophys Res* 119:1455–1483.
26. Heo J, Duc TA, Cho HS, Choi SU (2009) Characterization and prediction of meandering channel migration in the GIS environment: A case study of the Sabine River in the USA. *Environ Monit Assess* 152:155–165.
27. Blondeaux P, Seminara G (1985) A unified bar–bend theory of river meanders. *J Fluid Mech* 157:449–470.
28. D'Alpaos A, Lanzoni S, Marani M, Rinaldo A (2010) On the tidal prism-channel area relations. *J Geophys Res* 115:1–13.
29. Hickin EJ, Nanson GC (1975) The character of channel migration on the Beatton River, Northeast British Columbia, Canada. *Geol Soc Am Bull* 86:487–494.
30. Thorne CR (1991) Bank erosion and meander migration of the Red and Mississippi Rivers, USA. *Hydrology for the Water Management of Large River Basins: Proceedings of the Vienna Symposium*, eds van de Yen FHM, Gutknecht D, Loucks DP, Salewicz, KA (International Association of Hydrological Sciences, Wallingford, UK), pp 301–313.
31. Nanson GC, Hickin EJ (1986) A statistical analysis of bank erosion and channel migration in western Canada. *Geol Soc Am Bull* 97:497–504.
32. Furbish DJ (1988) River-bend curvature and migration: How are they related? *Geology* 16:752–755.
33. Blanckaert K (2011) Hydrodynamic processes in sharp meander bends and their morphological implications. *J Geophys Res* 116:1–22.
34. Hooke JM (1984) Changes in river meanders: A review of techniques and results of analyses. *Progr Phys Geogr* 8:473–508.
35. Crosato A (2009) Physical explanations of variations in river meander migration rates from model comparison. *Earth Surf Process Landforms* 34:155–161.
36. Parker G, Diplas P, Akiyama J (1983) Meander bends of high amplitude. *J Hydraulic Eng* 109:1323–1337.
37. Seminara G, Zolezzi G, Tubino M, Zardi D (2001) Downstream and upstream influence in river meandering. Part 2. Planimetric development. *J Fluid Mech* 438:213–230.
38. Lanzoni S, Seminara G (2006) On the nature of meander instability. *J Geophys Res* 111:1–14.
39. Güneralp I, Rhoads BL (2011) Influence of floodplain erosional heterogeneity on planform complexity of meandering rivers. *Geophys Res Lett* 38:L14401.
40. Parker G (1986) On the time development of meander bends. *J Fluid Mech* 162:139–156.
41. Güneralp I, Rhoads BL (2009) Empirical analysis of the planform curvature-migration relation of meandering rivers. *Water Resour Res* 45:W09424.
42. Fisher M, Barber M (1972) Scaling theory for finite-size effects in the critical region. *Phys Rev Lett* 28:1516–1519.
43. Leopold LB, Collins JN, Collins LM (1993) Hydrology of some tidal channels in estuarine marshland near San Francisco. *Catena* 20:469–493.
44. Lanzoni S, D'Alpaos A (2015) On funneling of tidal channels. *J Geophys Res* 120:433–452.
45. Dronkers J (1986) Tidal asymmetry and estuarine morphology. *Neth J Sea Res* 20:117–131.
46. Hughes ZJ, et al. (2009) Rapid headward erosion of marsh creeks in response to relative sea level rise. *Geophys Res Lett* 36:L03602.
47. Kinoshita R (1961) Investigation of channel deformation in Ishikari River (Bureau of Resources, Department of Science and Technology, Tokyo), Technical Report.
48. Eke EC, et al. (2014) Coevolution of width and sinuosity in meandering rivers. *J Fluid Mech* 760:127–174.
49. Marani M, et al. (2003) On the drainage density of tidal networks. *Water Resour Res* 39:1–11.
50. D'Alpaos A, et al. (2007) Spontaneous tidal network formation within a constructed salt marsh: Observations and morphodynamic modelling. *Geomorphology* 91:186–197.
51. Marani M, D'Alpaos A, Lanzoni S, Carniello L, Rinaldo A (2010) The importance of being coupled: Stable states and catastrophic shifts in tidal biomorphodynamics. *J Geophys Res* 115:F04004.
52. D'Alpaos A, et al. (2017) Tidal meander migration and dynamics: A case study from the Venice Lagoon. *Mar Petr Geol* 87:80–90.
53. Ghinassi M, et al. (December 21, 2018) Morphodynamic evolution and stratal architecture of translating tidal point bars: Inferences from the Northern Venice Lagoon (Italy). *Sedimentology*, 10.1111/sed.12425.
54. Bellucci LG, et al. (2007) ^{210}Pb and ^{137}Cs as chronometers for salt marsh accretion in the Venice Lagoon - links to flooding frequency and climate change. *J Environ Radioactivity* 97:85–102.
55. Giometto A, Altermatt F, Carrara F, Maritan A, Rinaldo A (2013) Scaling body size fluctuations. *Proc Natl Acad Sci USA* 110:4646–4650.